

# Hydrogen-Bond Mediated Electrocatalytic Nitrate Reduction to Ammonia over Metal-Organic Frameworks with Industrially Current Density

Xiao-Xue Fu,<sup>1,3#</sup> Hui Guo,<sup>1,3#</sup> Duan-Hui Si,<sup>1#</sup> Hong-Jing Zhu,<sup>1,3#</sup> Yi-Ying Lan,<sup>1</sup> Yuan-Biao Huang,<sup>1,2,3</sup> and Rong Cao<sup>1,2,3\*</sup>

<sup>1</sup>State Key Laboratory of Structural Chemistry, Fujian Institute of Research on the Structure of Matter, Chinese Academy of Sciences, Fujian, Fuzhou, 350002, P. R. China

<sup>2</sup>Fujian Science & Technology Innovation Laboratory for Optoelectronic Information of China Fuzhou, Fujian, 350108, P. R. China

<sup>3</sup>University of Chinese Academy of Sciences, Beijing 100049, P. R. China

Email: ybhuang@fjirsm.ac.cn (Y.-B. Huang), rcao@fjirsm.ac.cn (R. Cao)

# These authors contributed equally.

Content

|  |   |
|--|---|
| <b>1 Materials</b> .....   | 3 |
| <b>2 Synthesis of <math>\text{Cu}_3(\text{PyCA})_3</math></b> .....              | 3 |
| <b>3 Synthesis of <math>\text{Cu}_3(\text{Me-PyCA})_3</math></b> .....           | 3 |
| <b>4 Synthesis of DiMe-<math>\text{Cu}_3</math>-MOF</b> .....                    | 3 |
| <b>5 Synthesis of UniMe-<math>\text{Cu}_3</math>-MOF</b> .....                   | 4 |
| <b>6 Synthesis of NonMe-<math>\text{Cu}_3</math>-MOF</b> .....                   | 4 |
| <b>7 Characterization</b> .....  | 4 |
| <b>8 Electrochemical measurements</b> .....                                      | 5 |
| <b>9 Determination of ion concentration</b> .....                                | 6 |
| <b>10 <math>^{15}\text{N}</math> isotope labeling experiments</b> .....          | 6 |
| <b>11 Calculation of the Faradaic efficiency and yield rate of product</b> ..... | 7 |
| <b>12 Density Functional Theory (DFT) calculation</b> .....                      | 7 |

## Experimental Section

### 1 Materials

All reagents were purchased from commercial sources without further purification. 1H-pyrazole-4-amine (98%), 3,5-dimethyl-1H-pyrazole-4-carbaldehyde (98%), 3,5-Dimethyl-1H-pyrazol-4-amine (98%), Cu<sub>2</sub>O (98%), K<sup>15</sup>NO<sub>3</sub> (98 atom% <sup>15</sup>N), Sulfanilamide (C<sub>6</sub>H<sub>8</sub>N<sub>2</sub>O<sub>2</sub>S, 99%), N-(1-Naphthyl)Ethylenediamine Dihydrochloride (99%), were purchased from Adamas; 1H-pyrazole-4-carbaldehyde was purchased from Shanghai Bide Pharmaceutical Technology Co., Ltd; Cu(acac)<sub>2</sub>, 1,2-dichlorobenzene, *n*-Butanol was purchased from J&K Scientific Ltd; Cu(NO<sub>3</sub>)<sub>2</sub>·3H<sub>2</sub>O (99.7%), K<sub>2</sub>SO<sub>4</sub> (99.7%), KNO<sub>3</sub> (99.7%), were purchased from Sinopharm Chemical Reagent Co., Ltd; Deionized water was supplied with a UPT-I-5T ultrapure water system (18.3 MΩ cm).

### 2 Synthesis of Cu<sub>3</sub>(PyCA)<sub>3</sub>

Cu<sub>3</sub>(PyCA)<sub>3</sub> was synthesized according to a previously published procedure with slight modification. Detailly, Cu(NO<sub>3</sub>)<sub>2</sub>·3H<sub>2</sub>O (100 mg, 0.414 mmol) and 1H-pyrazole-4-carbaldehyde (PyCA, 50 mg, 0.5 mmol) were dissolved in a mixture of 3.35 mL N, N-dimethylformamide (DMF), 2.5 mL H<sub>2</sub>O and 3.35 mL ethanol in a 15 mL Pyrex tube. This blue-colored mixed solution was heated to 100 °C for 12 h. The collected light yellow crystalline product was washed with H<sub>2</sub>O and acetone for three times and dried at 70°C.

### 3 Synthesis of Cu<sub>3</sub>(Me-PyCA)<sub>3</sub>

Cu<sub>3</sub>(Me-PyCA)<sub>3</sub> was synthesized by mixing the ligand 3,5-dimethyl-1H-pyrazole-4-carbaldehyde (Me-PyCA, 13.9 mg, 0.125 mmol), Cupric(II) acetylacetonate (26.5 mg, 0.1 mmol), 2 mL ethanol, and 0.05 mL pyridine in a 15 mL Pyrex tube. This mixed solution was heated in an oven at 120°C for 72 h, and then slowly cooled to room temperature at a rate of -5 °C·h<sup>-1</sup>. Upon cooling to room temperature, the light brown crystalline product was collected in the bottom area of the tube, which were washed by H<sub>2</sub>O and acetone and dried under vacuum at 70°C. The successful synthesis of Cu<sub>3</sub>(Me-PyCA)<sub>3</sub> and Cu<sub>3</sub>(PyCA)<sub>3</sub> were confirmed by the PXRD, element analysis and FT-IR in Figure S21-S22 and Table S6-S8.

### 4 Synthesis of DiMe-Cu<sub>3</sub>-MOF

Cu<sub>3</sub>(Me-PyCA)<sub>3</sub> (28.0 mg, 0.05 mmol), Cu<sub>2</sub>O (10.7 mg, 0.075 mmol), 3,5-Dimethyl-1H-pyrazol-4-amine (DiMe-PyA, 16.7 mg, 0.15 mmol), 1,2-dichlorobenzene (1 mL), *n*-Butanol (0.5 mL) and 6 M aqueous acetic acid (0.1 mL) were added into a glass tube measuring 10 mm × 200 mm (o.d. × length). After sonication for 30 minutes the tube was flash frozen at 77 K (liquid N<sub>2</sub> bath). After three freeze-pump-thaw cycles, the system was evacuated to an internal

pressure of 50 mtorr and flame sealed. After recovering to RT, the mixture was heated at 120 °C and left undisturbed for 72 h. A pale precipitate was isolated by filtration in Buchner funnel and was washed with DMF and THF until the filtrate was colorless. The wet sample was transferred to a Soxhlet extractor and washed with MeOH (24 h). Finally, the product was evacuated at 70°C under dynamic vacuum overnight to yield activated sample.

## 5 Synthesis of UniMe-Cu<sub>3</sub>-MOF

Cu<sub>3</sub>(PyCA)<sub>3</sub> (23.7 mg, 0.05 mmol), Cu<sub>2</sub>O (10.7 mg, 0.075 mmol), 3,5-Dimethyl-1H-pyrazol-4-amine (DiMe-PyA, 16.7 mg, 0.15 mmol), 1,2-dichlorobenzene (1 mL), *n*-Butanol (0.5 mL) and 6 M aqueous acetic acid (0.1 mL) were added into a glass tube measuring 10 mm × 200 mm (o.d. × length). After sonication for 30 minutes the tube was flash frozen at 77 K (liquid N<sub>2</sub> bath). After three freeze-pump-thaw cycles, the system was evacuated to an internal pressure of 50 mtorr and flame sealed. After recovering to RT, the mixture was heated at 120 °C and left undisturbed for 72 h. A light green precipitate was isolated by filtration in Buchner funnel and was washed with DMF and THF until the filtrate was colorless. The wet sample was transferred to a Soxhlet extractor and washed with MeOH (24 h). Finally, the product was evacuated at 70°C under dynamic vacuum overnight to yield activated sample.

## 6 Synthesis of NonMe-Cu<sub>3</sub>-MOF

Cu<sub>3</sub>(PyCA)<sub>3</sub> (23.7 mg, 0.05 mmol), Cu<sub>2</sub>O (10.7 mg, 0.075 mmol), 1H-Pyrazol-4-amine (PyA, 12.5 mg, 0.15 mmol), 1,2-dichlorobenzene (1 mL), *n*-Butanol (0.5 mL) and 6 M aqueous acetic acid (0.1 mL) were added into a glass tube measuring 10 mm × 200 mm (o.d. × length). After sonication for 30 minutes the tube was flash frozen at 77 K (liquid N<sub>2</sub> bath). After three freeze-pump-thaw cycles, the system was evacuated to an internal pressure of 50 mtorr and flame sealed. After recovering to RT, the mixture was heated at 120 °C and left undisturbed for 72 h. A dark purple precipitate was isolated by filtration in Buchner funnel and was washed with DMF and THF until the filtrate was colorless. The wet sample was transferred to a Soxhlet extractor and washed with MeOH (24 h). Finally, the product was evacuated at 70°C under dynamic vacuum overnight to yield activated sample.

## 7 Characterization

Powder X-ray diffraction (PXRD) patterns were recorded on a Miniflex 600 diffractometer using Cu K $\alpha$  radiation ( $\lambda = 0.154$  nm). Infrared (IR) spectra were recorded using KBr pellets on a Bruker Optics VERTEX70 FT-IR Spectrometer. N<sub>2</sub> adsorption-desorption isotherm and the Brunauer-Emmett-Teller (BET) surface area measurements were measured by using Micromeritics ASAP 2460 instrument at 77 K. Solid-state <sup>13</sup>C NMR spectras was performed at AVANCE III BrukerBiospin spectrometer, operating at 400 MHz. Transmission electron microscopy (TEM) images and energy-dispersive X-ray spectroscopy (EDS) elemental distribution mapping were obtained with the FEI TECNAI

G2 F20 microscope equipped EDS detector. X-ray photoelectron spectroscopy (XPS) measurements were performed on an ESCALAB 250Xi X-ray photoelectron spectrometer (Thermo Fisher) using an Al Ka source (15 kV, 10 mA) and the binding energies were corrected through C 1s peak (284.6 eV). XAFS measurement and data analysis: XAFS spectra of the Cu K-edge were collected at BL14W1 station in Shanghai Synchrotron Radiation Facility (SSRF). The Cu K-edge XAFS data of pristine UniMe-Cu<sub>3</sub>-MOF was recorded in a transmission mode. UV-visible (UV/Vis) spectra were collected using a Shimadzu UV-2550 spectrophotometer at room temperature. Nuclear magnetic resonance (NMR) spectra were obtained on a JEOL JNM-ECZS 400S. ATR-FTIR experiments were performed on a Nicolet6700 (Thermo Fisher) equipped a liquid nitrogen cooled MCT detector. In situ Raman spectroscopy was performed on a Horiba Jobin Yvon Labram HR Evolution. The excitation source was a 532 nm laser.

## 8 Electrochemical measurements

The NO<sub>3</sub>RR experiments were executed on an electrochemical workstation (CHI 1140D, Chenhua, Shanghai) with a 30 mL H-type cell. The working electrode was Carbon paper (CP, 1×1 cm<sup>2</sup>) with DiMe-Cu<sub>3</sub>-MOF (or other contrast samples), reference electrode and counter electrode were Ag/AgCl/saturated KCl and Pt mesh (1×1 cm<sup>2</sup>). The electrochemical test was performed in 0.5 M K<sub>2</sub>SO<sub>4</sub> with 50 mM KNO<sub>3</sub> (25 mL in universal H-type cell) in both cathode and anode, and separated by a Nafion-117 proton exchange membrane.

**Working electrode preparation:** During electrochemical testing, the working electrodes for the three catalysts were prepared by drop-coating the catalyst ink (80 μL) onto carbon paper. The catalyst ink for all three catalysts was prepared using the following procedure: 5 mg of the catalyst and 2.5 mg ketjenblack was dispersed in 0.76 mL of isopropyl alcohol, 0.20 mL of ultrapure water and 40 μL of Nafion binder solution (5 wt%) under sonication for 1 h to form a homogeneous ink.

**In-situ infrared spectroscopy:** The test was conducted using a self-made ATR-FTIR in a mixed electrolyte of 0.5 M K<sub>2</sub>SO<sub>4</sub> and 50 mM KNO<sub>3</sub>. An Ag/AgCl electrode was used as the reference electrode, and the electrochemical nitrate reduction reaction was performed on a glassy carbon electrode. The working electrode must be in contact with the Ge crystal surface so that the infrared beam can detect the intermediate species formed during the nitrate reduction process. First, the electrochemical cell was bubbled with Ar for 30 minutes, and then Ar was continuously introduced during the test. Afterwards, we conducted a background infrared spectral analysis. Then, a reaction potential was applied to the working electrode, and real-time spectra with a resolution of 4 cm<sup>-1</sup> were collected, with a total of 32 interferograms added to each spectrum and a collection period of 30 seconds.

**In-situ Raman spectroscopy:** Raman spectroscopy was performed with a LabRAM HR Evolu Raman microscopy system equipped with a 532 nm laser as the excitation source. Each spectrum is an average of five continuously acquired spectra with a collection time of 50s each. The test was conducted using a Gas diffusion electrode in a mixed electrolyte of 0.5 M  $K_2SO_4$  and 50 mM  $KNO_3$ , and Pt wires and a Ag/AgCl electrode were used as counter and reference electrodes, respectively.

## 9 Determination of ion concentration

The ultraviolet-visible (UV-Vis) spectrophotometer was used to detect the ion concentration of post-test electrolytes after diluting to appropriate concentration to match the range of calibration curves. The specific detection methods are as follow:

Determination of ammonia-N:

The  $NH_4^+$  concentration in liquid products was quantified via an indophenol blue method. In a typical process, liquid products were obtained after the consecutive electrolysis at a specific potential for 2 h, and the liquid products were diluted by deionized water to ensure the  $NH_4^+$  concentration locate at the linear range of standard curves. Specifically, 10.0 mL of the diluted electrolyte was taken and further mixed with 0.50 ml of a 5.0 wt % Salicylic acid solution. Then, 0.1 mL of 1.0 wt %  $C_5FeN_6Na_2O$  and 0.1 ml of 0.05 wt % NaClO were added to the above solution. After standing at room temperature for 1 h, the UV-Vis absorption spectrum was measured. The concentrations of  $NH_4^+$  were determined using the absorbance around the wavelength of 697 nm. In addition, Ion Chromatography (IC) was used to verify the accuracy of the UV-Vis method.

Determination of nitrite-N:

A mixture of Sulfanilamide ( $NH_2C_6H_4SO_2NH_2$ , 1.0 g), N-(1-Naphthyl)Ethylenediamine Dihydrochloride ( $C_{10}H_7NHC_2H_4NH_2 \cdot 2HCl$ , 0.1 g), ultrapure water (25 mL) and phosphoric acid (5 mL,  $\rho=1.70$  g/mL) was used as a color reagent. A certain amount of electrolyte was taken out from the electrolytic cell and diluted to 5 mL to detection range. Next, 0.1 mL color reagent was added into the 5 mL solution and mixed uniformly, and the absorption intensity at a wavelength of 540 nm was recorded after sitting for 20 min. The concentration-absorbance curve was calibrated using a series of standard sodium nitrite solutions.

## 10 $^{15}N$ isotope labeling experiments

The electrochemical nitrate reduction method was used for the isotopically labelled nitrate reduction experiments, except that the nitrogen source was changed to 98 atom%  $K^{15}NO_3$ . Taking  $^{15}NH_4^+$  as an example, the specific steps

were as follows: After electroreduction, electrolyte with obtained  $^{15}\text{NH}_4^+$  -  $^{15}\text{N}$  was taken out and the pH value was adjusted to 1~2 with 4.0 M  $\text{H}_2\text{SO}_4$  for further quantification by  $^1\text{H}$  NMR (JEOL JNM-ECZS 400S). Then 0.5 mL of the above solution was detected by NMR with adding 50  $\mu\text{L}$   $\text{D}_2\text{O}$ .

## 11 Calculation of the Faradaic efficiency and yield rate of product

The FE of  $\text{NH}_3$  was calculated using Equation 1:

$$FE = (8 \times F \times C_{\text{NH}_3} \times V) / (17 \times Q) \times 100\% \quad (1)$$

The yield rate ( $\mu\text{g}_{\text{NH}_3} \cdot \text{cm}^{-2} \cdot \text{h}^{-1}$ ) of  $\text{NH}_3$  can be calculated using the following equation (Equation 2):

$$\text{Yield rate}(\text{NH}_3) = (C_{\text{NH}_3} \times V) / (t \times A) \quad (2)$$

The FE of  $\text{NO}_2^-$  was calculated using Equation 3:

$$FE = (2 \times F \times C_{\text{NO}_2-\text{N}} \times V) / (14 \times Q) \times 100\% \quad (3)$$

where  $C_{\text{NH}_3}$  is the measured N of  $\text{NO}_2^-$  concentration ( $\text{g} \cdot \text{mL}^{-1}$ ); V is the volume of the electrolyte (25 mL);  $C_{\text{NO}_2-\text{N}}$  is the measured  $\text{NH}_3$  concentration ( $\text{g} \cdot \text{mL}^{-1}$ ); t is the electrolysis time (2 h); A is the geometric area of the electrode (1  $\text{cm}^2$ ); F is the faraday constant ( $96485 \text{ C mol}^{-1}$ ); Q (C) Q is the total charge passing through the electrode.

## 12 Density Functional Theory (DFT) calculation

To reveal the speculation of the effects of hydrogen bonding on  $\text{NO}_3\text{RR}$ , the mechanism of  $\text{NO}_3\text{RR}$  on the DiMe- $\text{Cu}_3$ -MOF and NonMe- $\text{Cu}_3$ -MOF were calculated by density functional theory (DFT) through Vienna Ab initio Simulation Package (VASP) <sup>1-4</sup>. The Projector Augmented Wave (PAW) <sup>5,6</sup> in conjunct with the Perdew-Burke-Ernzerh (PBE) flavor <sup>7</sup> were carried out in all calculations. The k-point sampling of (2,2,1) for DiMe- $\text{Cu}_3$ -MOF and NonMe- $\text{Cu}_3$ -MOF were employed. The convergence criteria and the cutoff energy of plane wave basis was set to  $1 \times 10^{-4}$  eV and 400 eV, respectively. The threshold for force was set to  $-0.05 \text{ eV} \cdot \text{\AA}^{-1}$ , and the Van der Waals (vdW) correction was adopted by Grimme (DFT+D3) <sup>8</sup>.

The DiMe- $\text{Cu}_3$ -MOF and NonMe- $\text{Cu}_3$ -MOF were modeled using three layers slab, respectively. The top layer and the adsorbates were fully relaxed, and the remaining layers were fixed. To avoid the periodic interactions of the system, a vacuum region of 18  $\text{\AA}$  between two repeated slabs was used in the direction perpendicular to the surface. The free energies of all intermediates of the electrochemical reactions were calculated by the computational hydrogen electrode

model<sup>9</sup>. The  $\Delta G_0$  was calculated at 298.15 K by the VASPKIT package<sup>10</sup>, which according to  $\Delta G_0 = \Delta E_{\text{DFT}} + \Delta E_{\text{ZPE}} - T\Delta S$ . The  $E_{\text{DFT}}$ ,  $E_{\text{ZPE}}$  and  $S$  indicates the electronic energy, zero-point energy and entropy, respectively.

## Figures and Tables

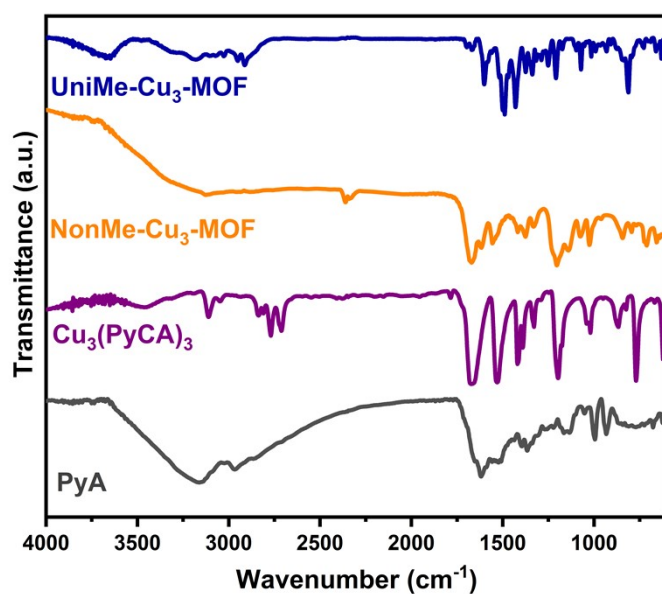


**Figure S1.** The FT-IR spectra of PyA,  $\text{Cu}_3(\text{PyCA})_3$ , UniMe- $\text{Cu}_3$ -MOF and NonMe- $\text{Cu}_3$ -MOF.

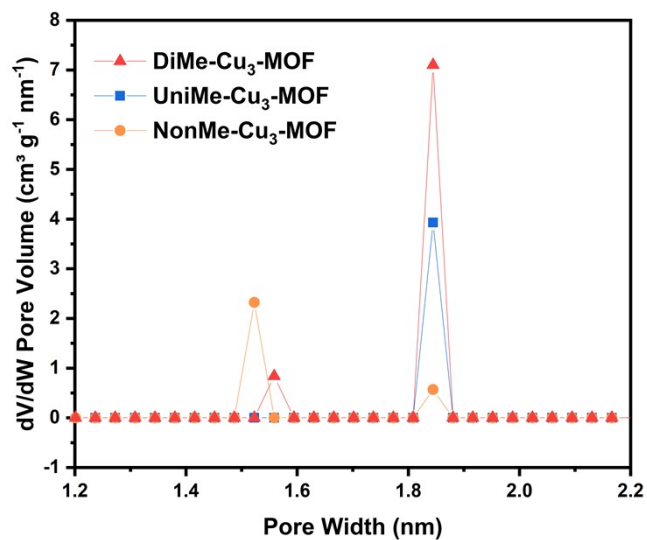


**Figure S2.** The pore distribution of UniMe- $\text{Cu}_3$ -MOF, NonMe- $\text{Cu}_3$ -MOF and DiMe- $\text{Cu}_3$ -MOF.

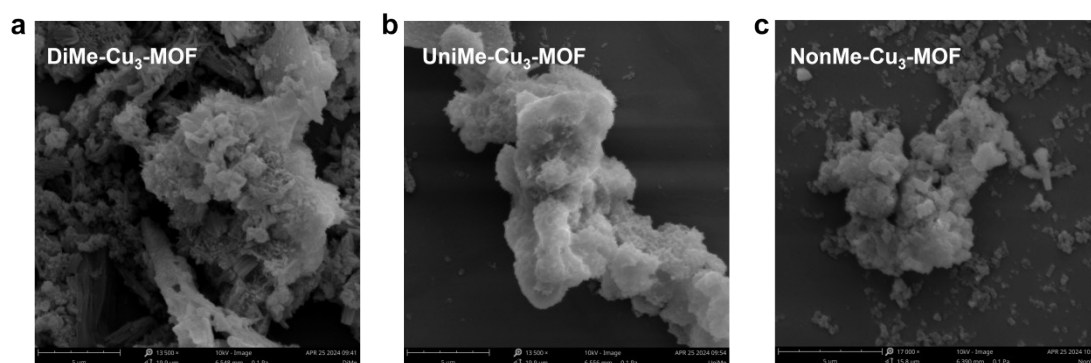


**Figure S3.** The scanning electron microscopy (SEM) images of (a) DiMe-Cu<sub>3</sub>-MOF. (b) UniMe-Cu<sub>3</sub>-MOF. (c) NonMe-Cu<sub>3</sub>-MOF.

**Table S1.** Cu K-edge EXAFS curve fitting parameters of DiMe-Cu<sub>3</sub>-MOF. CN, coordination number; R, distance between absorber and backscatterer atoms;  $\sigma^2$ , Debye-Waller factor (a measure of thermal and static disorder in absorber-scatterer distances); R factor is used to value the goodness of the fitting.

| Sample                    | Path | CN  | R (Å) | $\sigma^2$ ( $10^{-3}\text{Å}^2$ ) | R factor |
|---------------------------|------|-----|-------|------------------------------------|----------|
| DiMe-Cu <sub>3</sub> -MOF | Cu-N | 2.0 | 1.85  | 4±0.003                            | 0.02     |

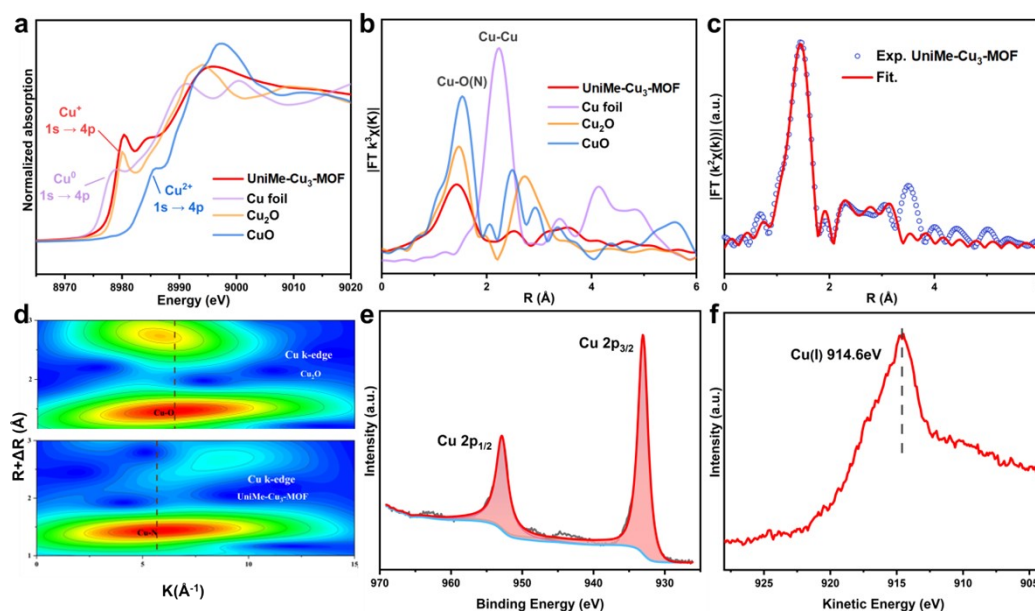


**Figure S4.** (a) Cu K-edge of XANES spectra of UniMe-Cu<sub>3</sub>-MOF, Cu foil, CuO and Cu<sub>2</sub>O. (b) Cu K-edge of EXAFS spectra of UniMe-Cu<sub>3</sub>-MOF, Cu foil, CuO and Cu<sub>2</sub>O. (c) The EXAFS fitting curves of UniMe-Cu<sub>3</sub>-MOF. (d) WT-EXAFS plots of UniMe-Cu<sub>3</sub>-MOF and Cu<sub>2</sub>O. (e) Cu 2p XPS spectra and (f) Cu LMM Auger spectra of UniMe-Cu<sub>3</sub>-MOF.

**Table S2.** Cu K-edge EXAFS curve fitting parameters of UniMe-Cu<sub>3</sub>-MOF. CN, coordination number; R, distance between absorber and backscatter atoms;  $\sigma^2$ , Debye-Waller factor (a measure of thermal and static disorder in absorber-scatterer distances); R factor is used to value the goodness of the fitting

| Sample                     | Path | CN  | R (Å) | $\sigma^2$ ( $10^{-3}\text{Å}^2$ ) | R factor |
|----------------------------|------|-----|-------|------------------------------------|----------|
| UniMe-Cu <sub>3</sub> -MOF | Cu-N | 2.0 | 1.85  | 3.6±1.7                            | 0.02     |

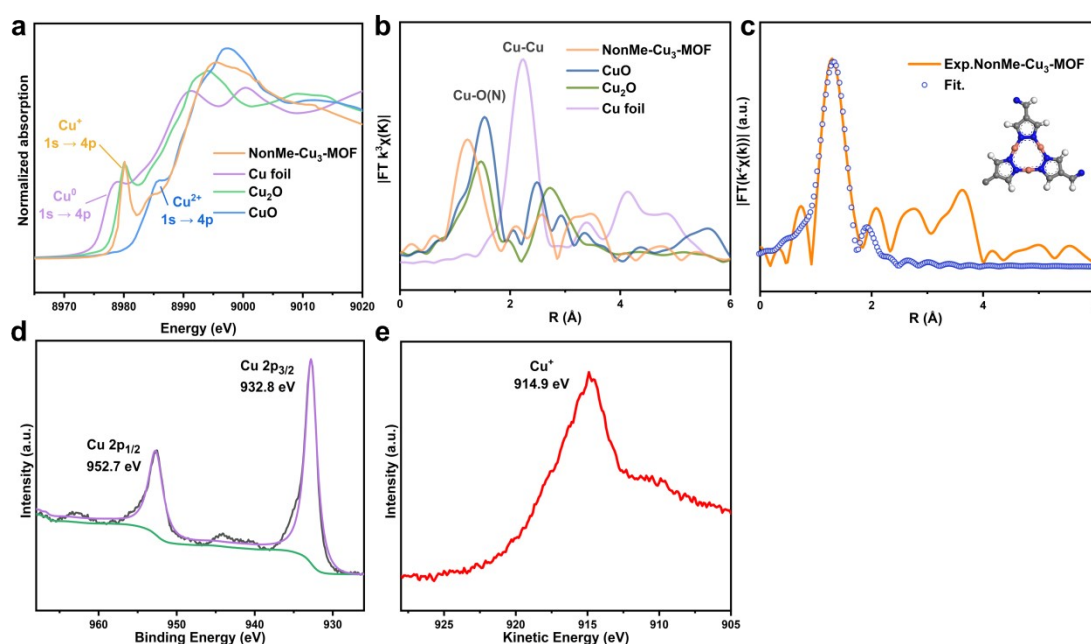


**Figure S5.** (a) Cu K-edge of XANES spectra of NonMe-Cu<sub>3</sub>-MOF, Cu foil, CuO and Cu<sub>2</sub>O. (b) Cu K-edge of EXAFS spectra of NonMe-Cu<sub>3</sub>-MOF, Cu foil, CuO and Cu<sub>2</sub>O. (c) The EXAFS fitting curves of NonMe-Cu<sub>3</sub>-MOF. (d) Cu 2p XPS spectra and (e) Cu LMM Auger spectra of NonMe-Cu<sub>3</sub>-MOF.

**Table S3.** Cu K-edge EXAFS curve fitting parameters of NonMe-Cu<sub>3</sub>-MOF. CN, coordination number; R, distance between absorber and backscatterer atoms;  $\sigma^2$ , Debye-Waller factor (a measure of thermal and static disorder in absorber-scatterer distances); R factor is used to value the goodness of the fitting.

| Sample                     | Path | CN  | R (Å) | $\sigma^2$ ( $10^{-3}\text{Å}^2$ ) | R factor |
|----------------------------|------|-----|-------|------------------------------------|----------|
| NonMe-Cu <sub>3</sub> -MOF | Cu-N | 2.0 | 1.83  | 9.5±2.7                            | 0.03     |

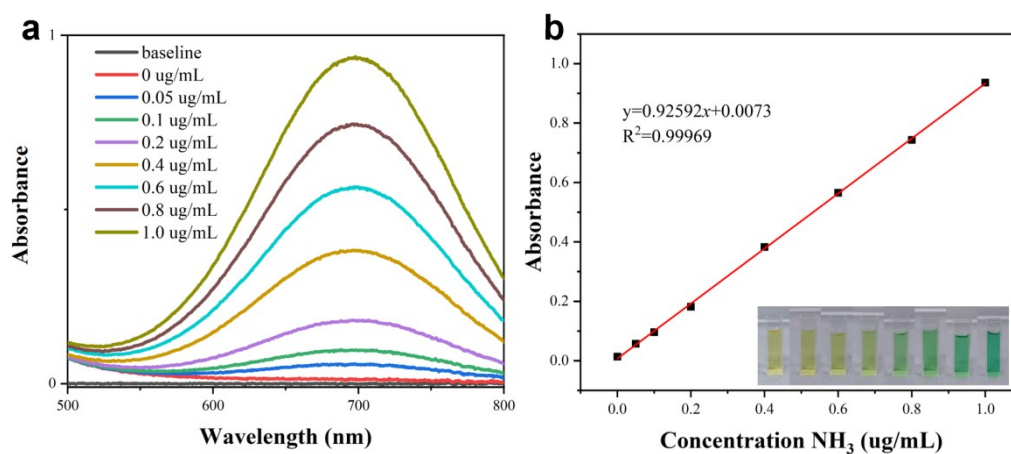


**Figure S6.** (a) UV-Vis curves of NH<sub>4</sub>Cl solutions with known concentration as standards, and (b) the corresponding linear standard curve.

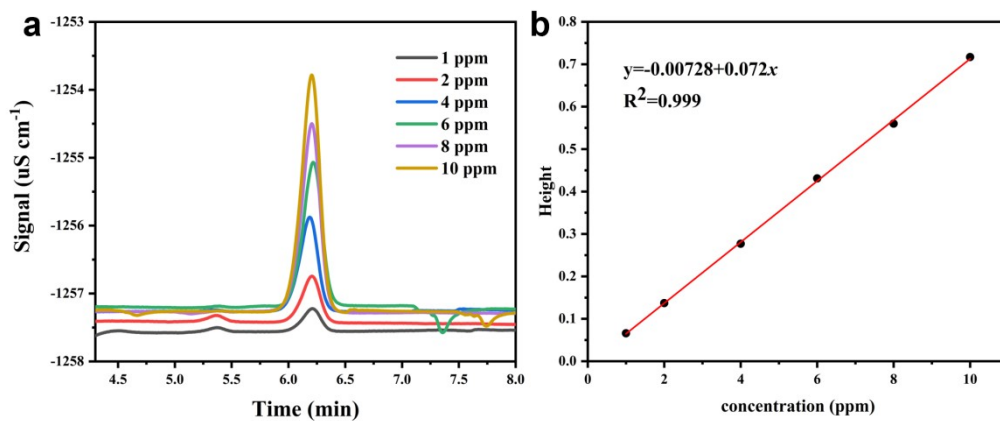


**Figure S7.** (a) IC curves of  $\text{NH}_4\text{Cl}$  solutions with known concentration as standards, and (b) the corresponding linear standard curve.

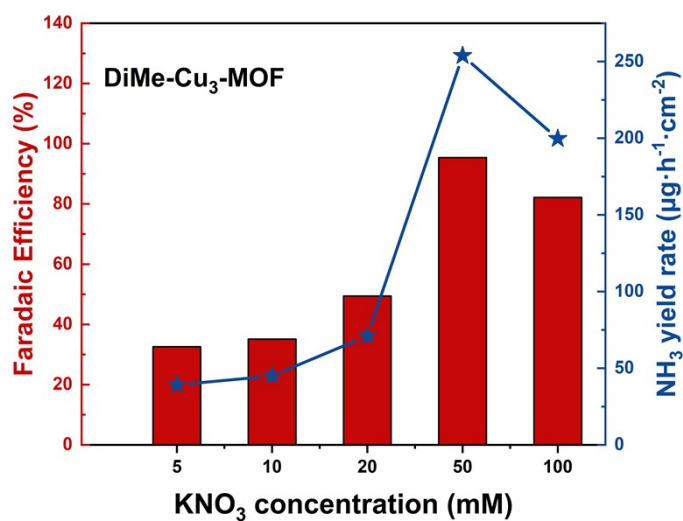


**Figure S8.** The  $\text{NH}_3$  yield of DiMe- $\text{Cu}_3$ -MOF under different  $\text{KNO}_3$  concentration.

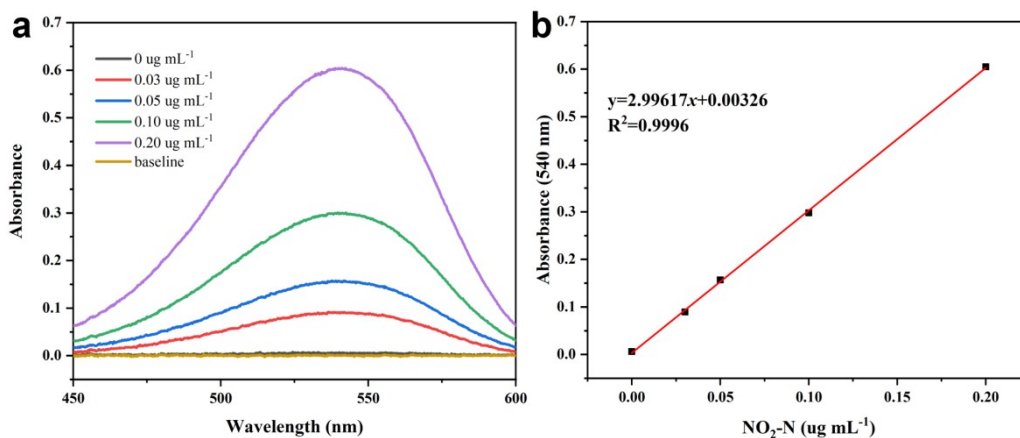


**Figure S9.** (a) UV-Vis curves of  $\text{KNO}_2$  solutions with known concentration as standards. (b) The linear standard curve for estimation of  $\text{NO}_2\text{-N}$  consumption.

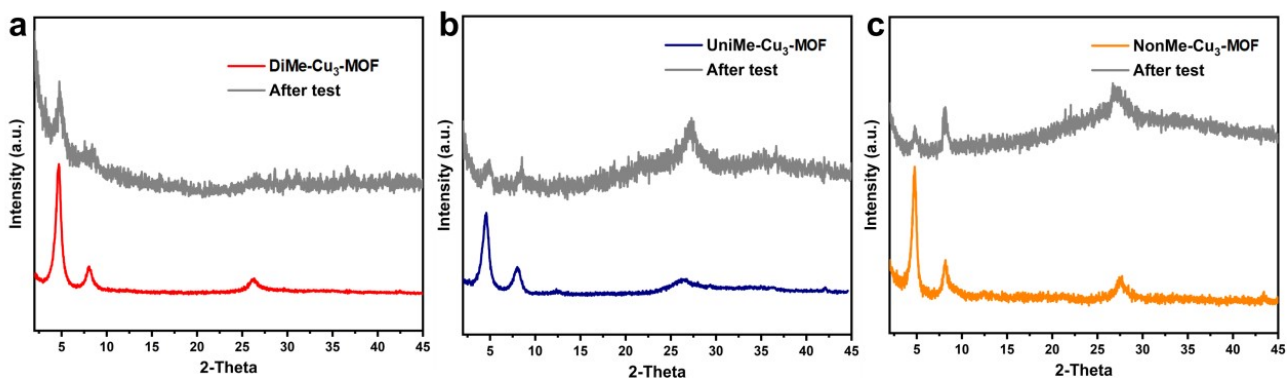


**Figure S10.** (a) PXRD pattern of DiMe- $\text{Cu}_3\text{-MOF}$  after test. (b) PXRD pattern of UniMe- $\text{Cu}_3\text{-MOF}$  after test. (c) PXRD pattern of NonMe- $\text{Cu}_3\text{-MOF}$  after test.

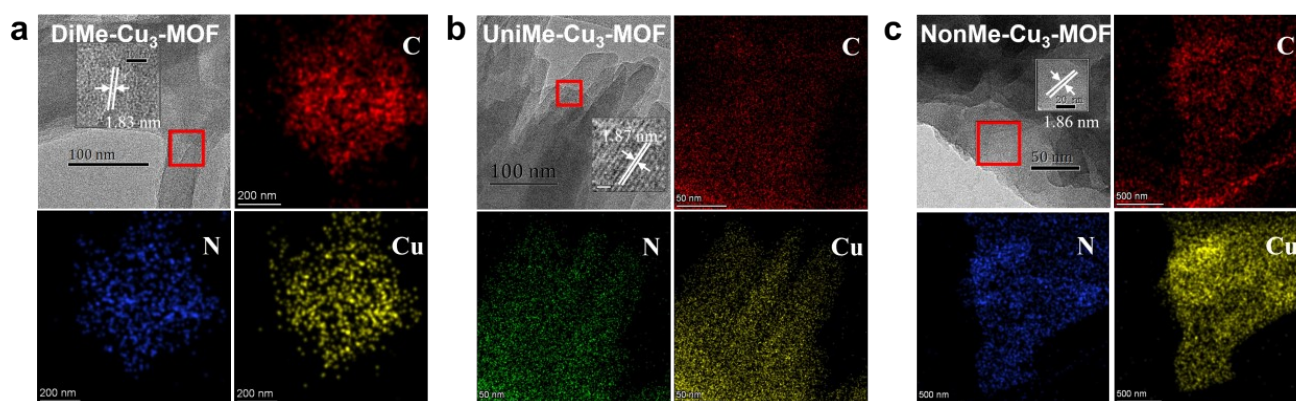


**Figure S11.** (a) TEM image of DiMe- $\text{Cu}_3\text{-MOF}$  after test, (b) TEM image of UniMe- $\text{Cu}_3\text{-MOF}$  after test and (c) TEM image of NonMe- $\text{Cu}_3\text{-MOF}$ .

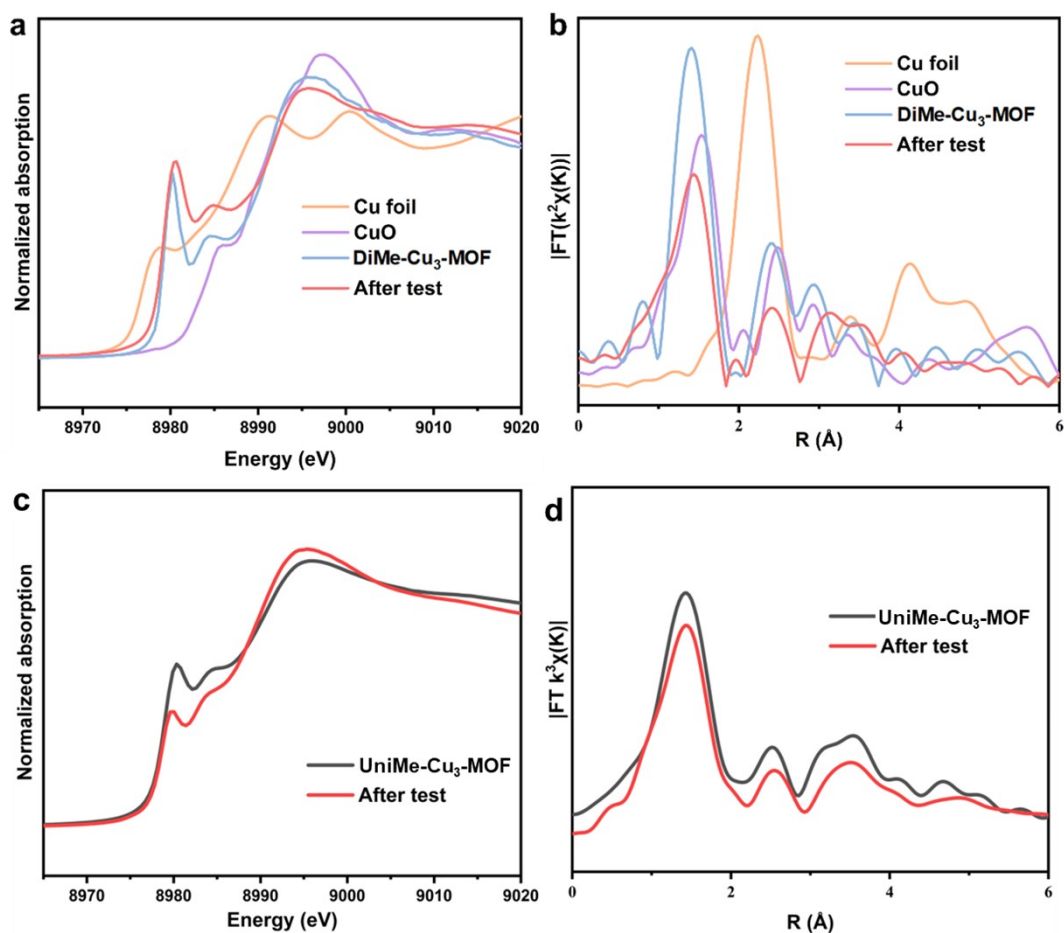


**Figure S12.** (a) The Cu K-edge of XANES spectra of DiMe-Cu<sub>3</sub>-MOF after test, Cu foil and CuO. (b) Cu K-edge of EXAFS spectra of DiMe-Cu<sub>3</sub>-MOF after test, Cu foil and CuO. (c) Cu K-edge of XANES spectra and (d) Cu K-edge of EXAFS spectra of UniMe-Cu<sub>3</sub>-MOF after test.

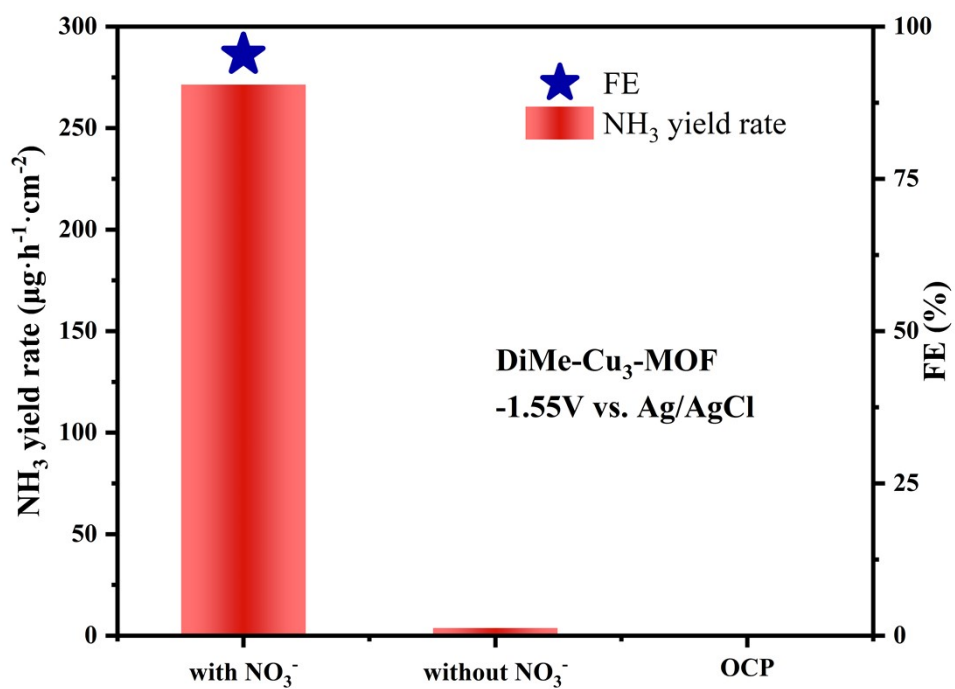
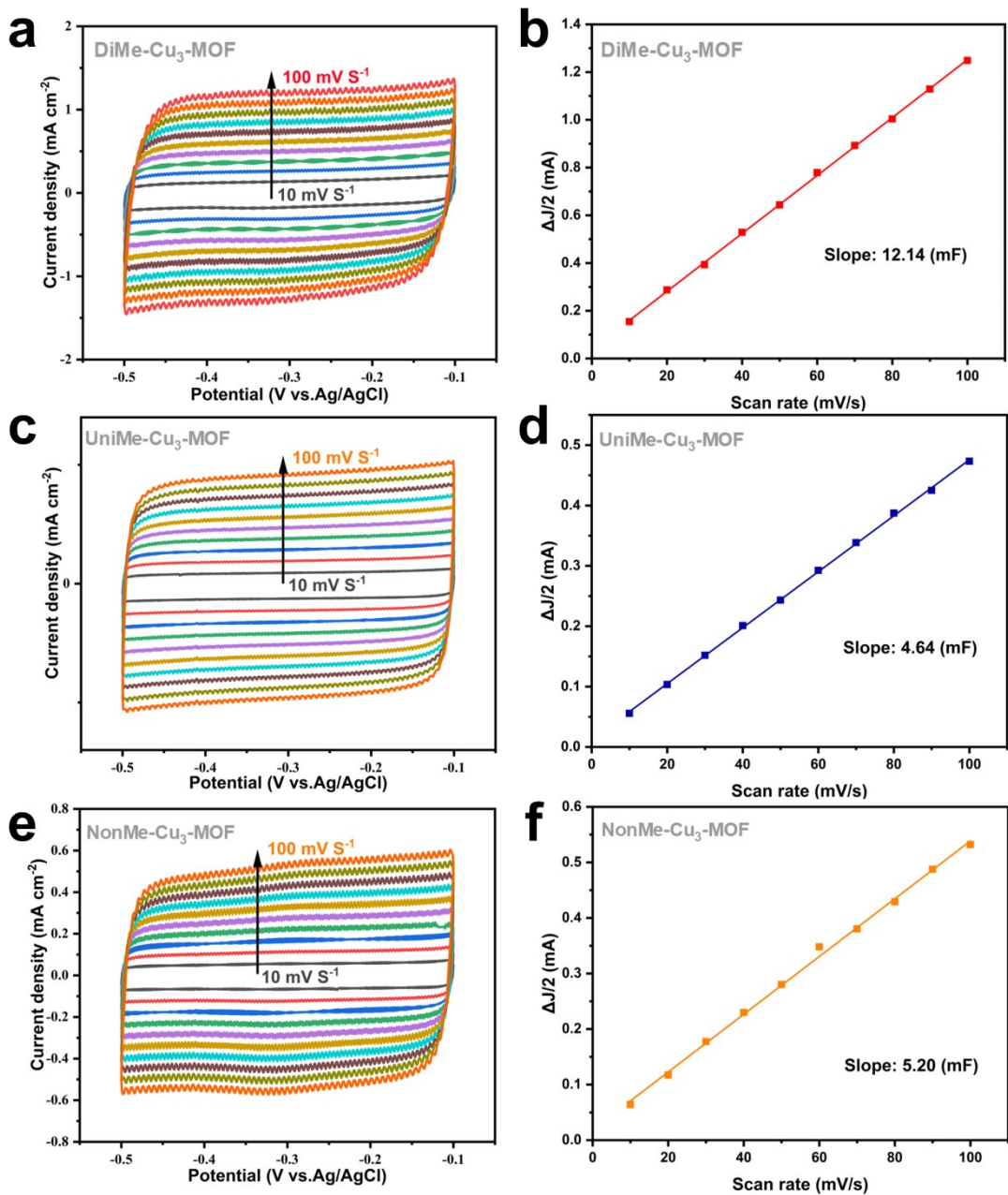
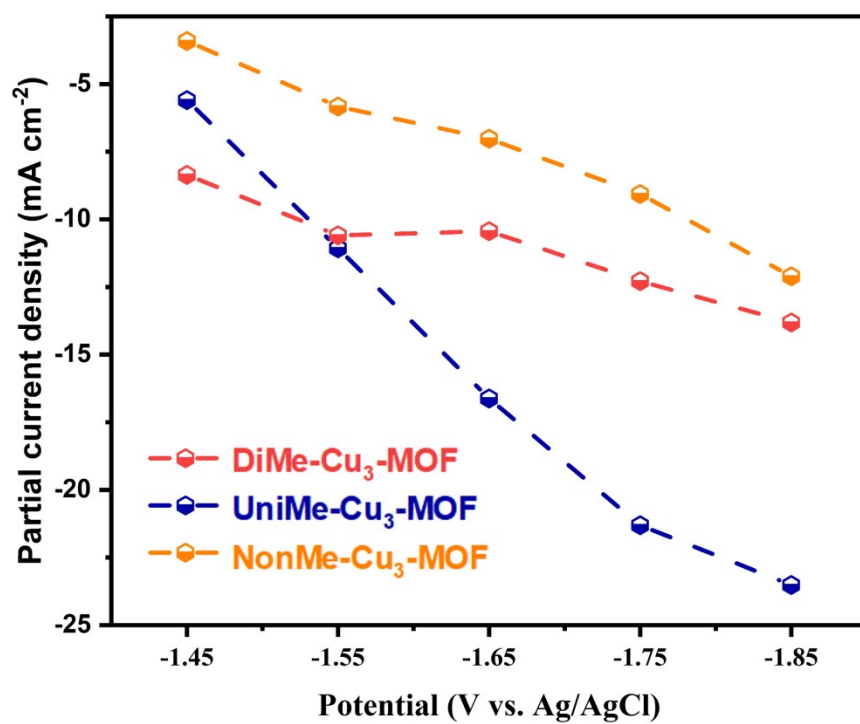


Figure S13. NO<sub>3</sub>RR performance of DiMe-Cu<sub>3</sub>-MOF with different conditions.



**Figure S14.** CV scan rate-current relationship and the corresponding electrochemical active surface area (ECSA) analysis of (a-b) DiMe-Cu<sub>3</sub>-MOF, (c-d) UniMe-Cu<sub>3</sub>-MOF and (e-f) NonMe-Cu<sub>3</sub>-MOF.



**Figure S15.** The partial current densities of  $\text{NH}_3$  evolution for different catalysts with 50 mM  $\text{KNO}_3$  after ECSA normalization.

**Table S4.** ECSA analysis results of DiMe-Cu<sub>3</sub>-MOF, UniMe-Cu<sub>3</sub>-MOF, and NonMe-Cu<sub>3</sub>-MOF.

| Sample                     | $C_{dl}$ (mF) | ECSA ( $\text{cm}^2$ ) |
|----------------------------|---------------|------------------------|
| DiMe-Cu <sub>3</sub> -MOF  | 12.14         | 202.33                 |
| UniMe-Cu <sub>3</sub> -MOF | 4.64          | 77.33                  |
| NonMe-Cu <sub>3</sub> -MOF | 5.20          | 86.67                  |

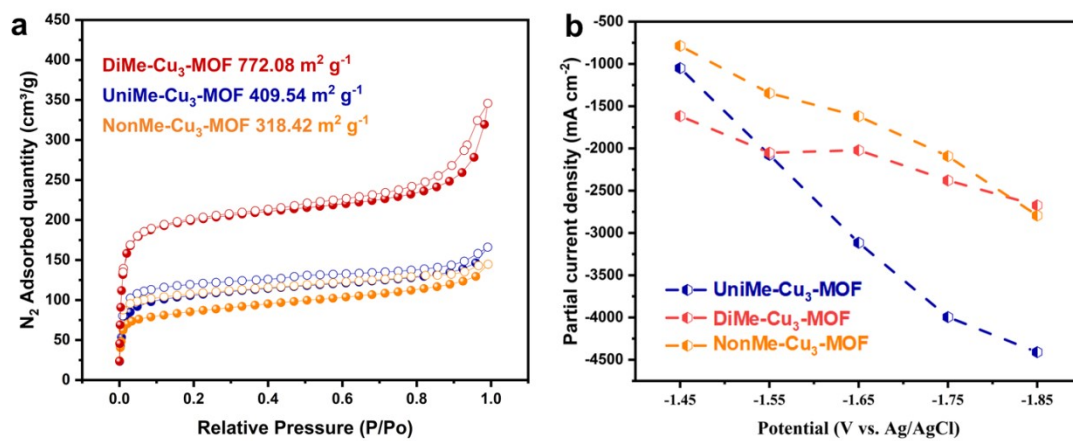


**Figure S16.** (a)  $N_2$  adsorption for NonMe- $Cu_3$ -MOF, UniMe- $Cu_3$ -MOF and DiMe- $Cu_3$ -MOF. (b) The partial current densities of  $NH_3$  evolution for different catalysts with 50 mM  $KNO_3$  after BET normalization.

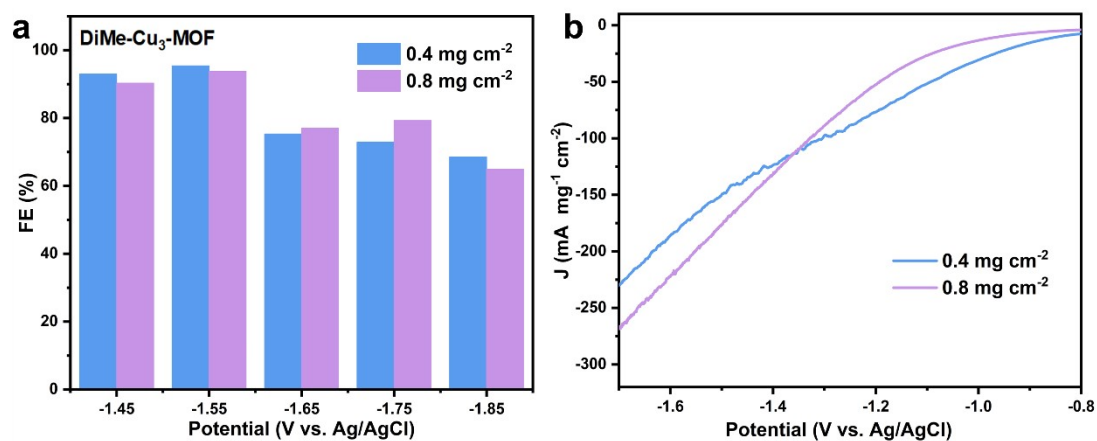


**Figure S17.** (a) Ammonia Faraday efficiency under different DiMe- $Cu_3$ -MOF loading, (b) normalized LSV curves under different DiMe- $Cu_3$ -MOF loading.



**Figure S18.** Device photo of in-situ FTIR.

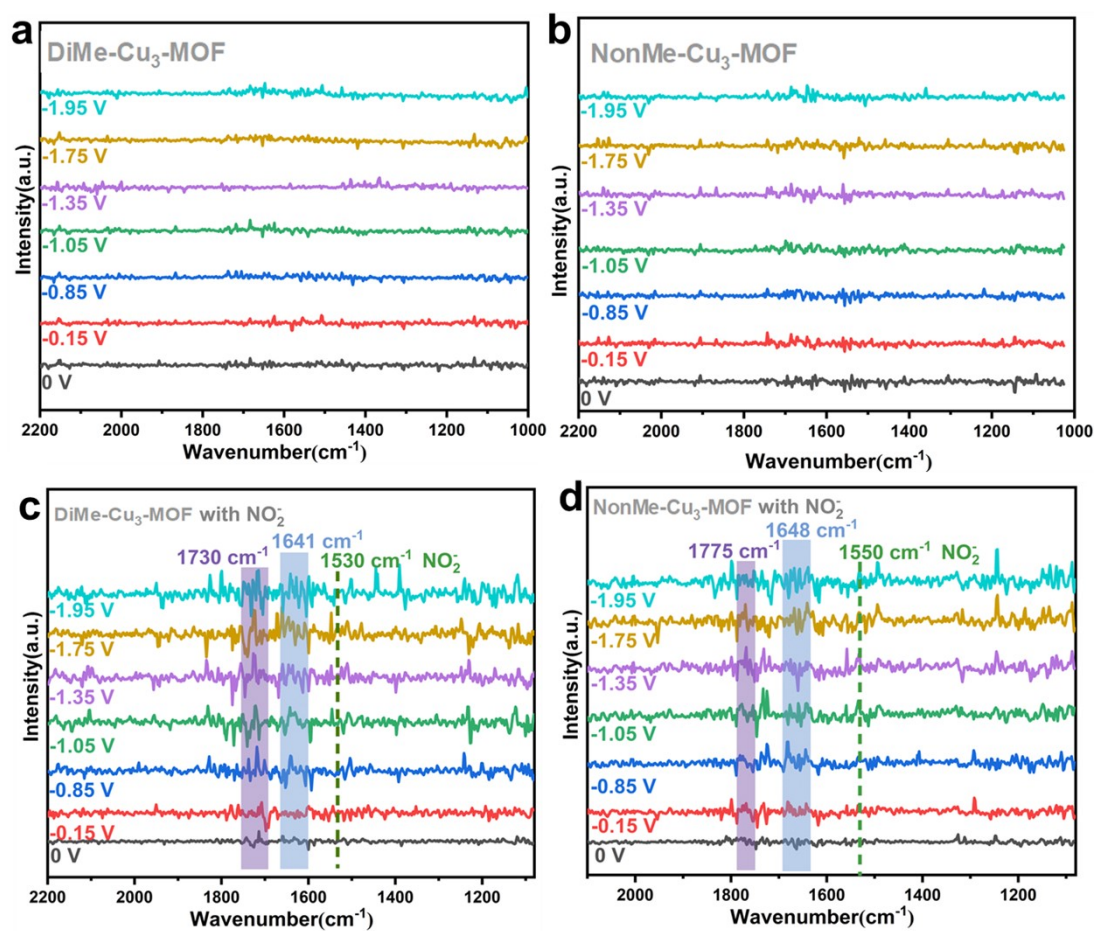


**Figure S19.** (a, b) In-situ FTIR spectra under the catalysts without nitrate anions of (a) DiMe-Cu<sub>3</sub>-MOF and (b) NonMe-Cu<sub>3</sub>-MOF. (c, d) In-situ FT-IR spectra under the catalysts with nitrite anions of (a) DiMe-Cu<sub>3</sub>-MOF and (b) NonMe-Cu<sub>3</sub>-MOF.

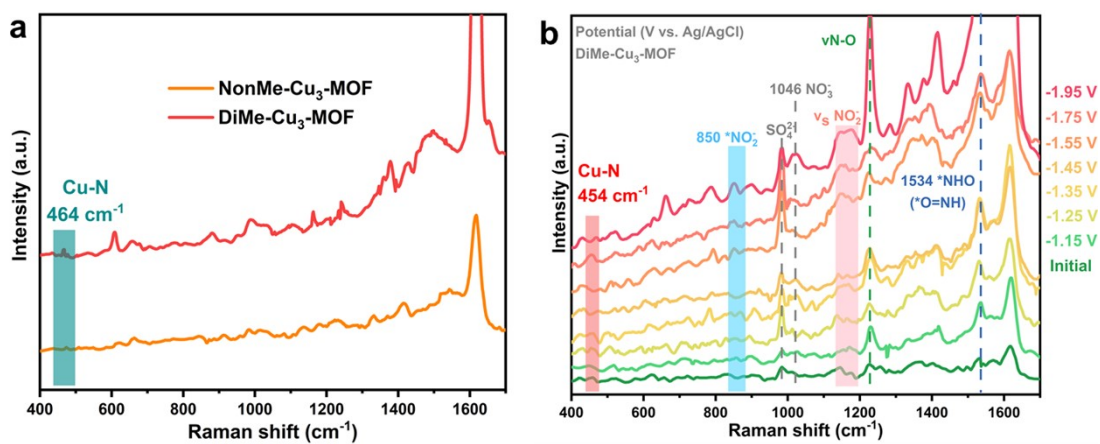


**Figure S20.** (a) Raman spectra of DiMe-Cu<sub>3</sub>-MOF and NonMe-Cu<sub>3</sub>-MOF. (b) Enlarged in-situ Raman spectrum of DiMe-Cu<sub>3</sub>-MOF.

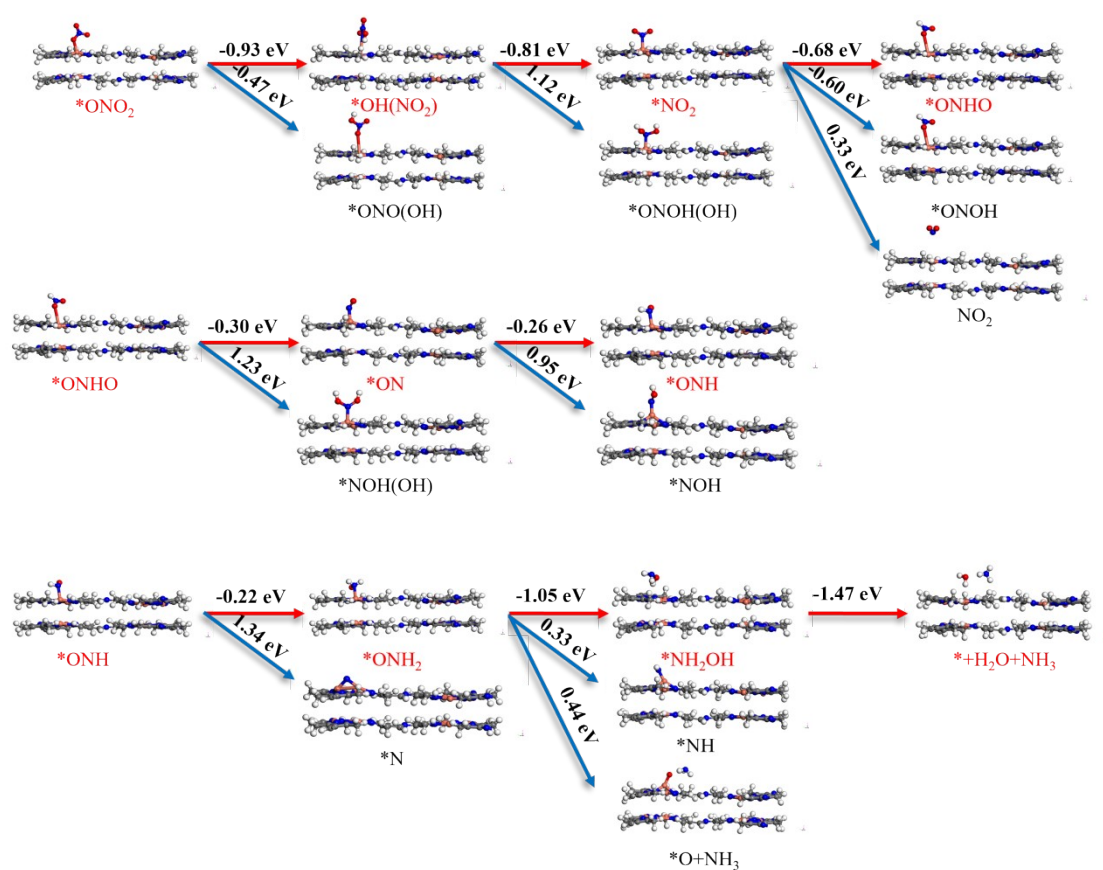


**Figure S21.** The probable pathway of NO<sub>3</sub>RR on DiMe-Cu<sub>3</sub>-MOF (side view).

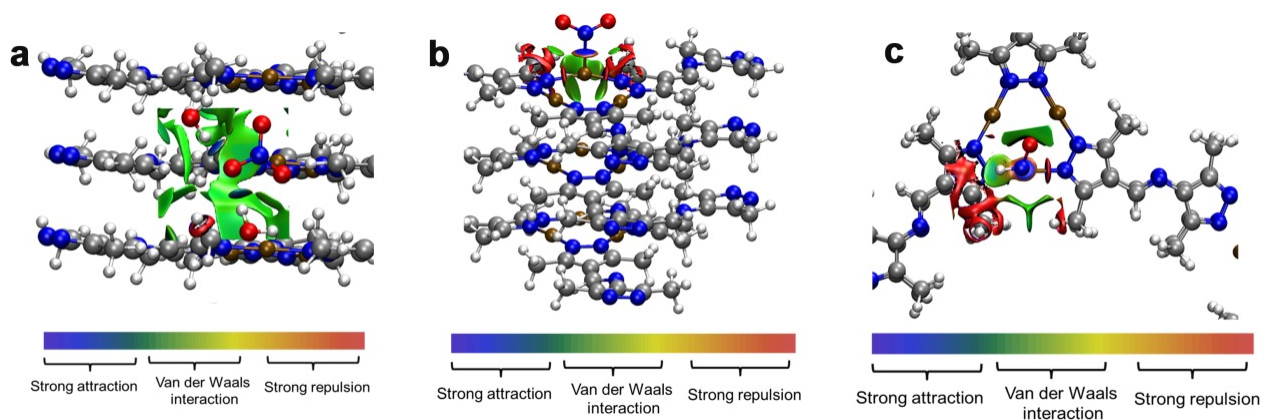


**Figure S22.** The noncovalent interaction (NCI) between (a)  $-\text{CH}_3$  and  $^*\text{NO}_3\text{---H}_2\text{O}$ ; (b)  $-\text{CH}_3$  and  $^*\text{NO}_2$  and (c)  $-\text{CH}_3$  and  $^*\text{ONH}$ .

**Table S5.** Performance of Cu-based Electrocatalysts and MOFs/COFs Electrocatalysts for the Reduction of Nitrate to Ammonia.

| Catalyst                  | Electrolyte  | $\text{NH}_3$<br>Faradaic<br>efficiency<br>/% | $\text{NH}_3$<br>partial<br>current<br>density<br>/mA cm <sup>-2</sup> | $\text{NH}_3$ yield<br>rate<br>/mmol h <sup>-1</sup><br>cm <sup>-2</sup> | Potential/V<br>vs. Ag/AgCl | References   |
|---------------------------|--|---|--|--|----------------------------|--|
| DiMe-Cu <sub>3</sub> -MOF | 50 mM KNO <sub>3</sub> +<br>0.5 M K <sub>2</sub> SO <sub>4</sub>   | 95  | 86   | 0.44   | -1.55                      | This work  |
|                           | 0.5 M KNO <sub>3</sub> +<br>0.5 M K <sub>2</sub> SO <sub>4</sub>   | 80  | 960  | 17.73  |                            | This work  |
| CuPOR-COF                 | 1 M KNO <sub>3</sub> + 1<br>M KOH                                  | 86  | 86   | 0.35   | -1.7                       | <i>Adv. Mater.</i> <b>2023</b> ,<br>36 (14), 2309302.<br>11    |
| Mo HATN-COFs              | 0.1 M NaNO <sub>3</sub> +<br>0.1 M Na <sub>2</sub> SO <sub>4</sub> | 96  | 61   | 0.50   | -0.8                       | <i>Green. Chem.</i><br><b>2023</b> , 25 (22),<br>9167-9174. 12 |
| PPy-Cu-E                  | 0.4 M K <sub>2</sub> SO <sub>4</sub> +<br>0.2 M KNO <sub>3</sub>   | 92  | 70   | 0.35   | -1.0                       | <i>Green. Chem.</i><br><b>2023</b> , 25 (22),<br>9167-9174. 13 |
| FOSP-Cu-0.1               | 0.5 M Na <sub>2</sub> SO <sub>4</sub><br>+ 0.1 M KNO <sub>3</sub>  | 94  | 70   | 0.10   | -0.68                      | <i>Nano Energy.</i><br><b>2022</b> , 97 107124.<br>14          |
| Cu/Cu <sub>2</sub> O NWAs | 200 ppm NO <sub>3</sub> <sup>-</sup><br>+ 0.5 M                    | 96  | 109  | 0.245  | -1.26                      | <i>Angew. Chem. Int.</i><br><i>Ed.</i> <b>2020</b> , 59 (13),  |

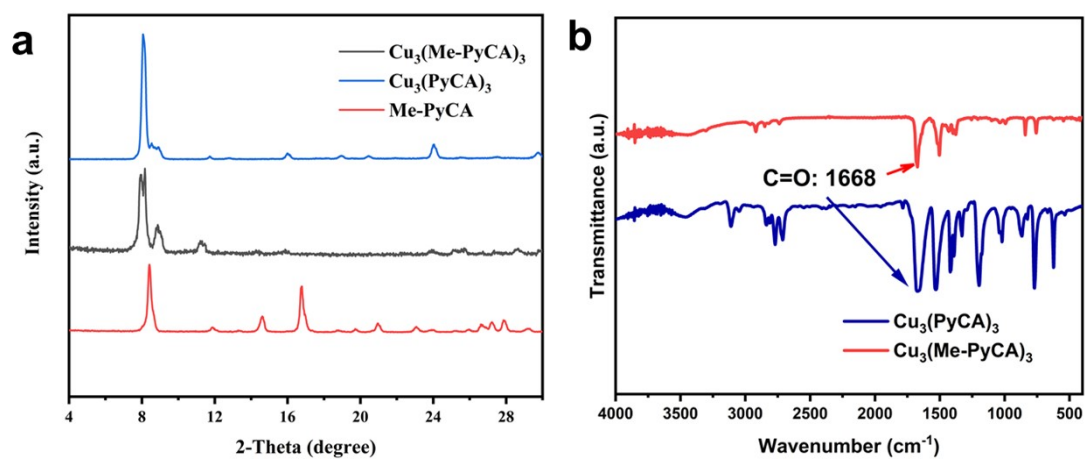
|                                     |   |    |      |       |       |   |
|-------------------------------------|---|----|------|-------|-------|---|
|                                     | Na <sub>2</sub> SO <sub>4</sub>   |    |      |       |       | 5350-5354. <sup>15</sup>  |
| Fe <sub>2</sub> Co-MOF              | 0.051 M H <sub>2</sub> SO <sub>4</sub><br>+ 50 g L <sup>-1</sup><br>KNO <sub>3</sub>              | 82 | 23   | 0.079 | -1.2  | <i>Angew. Chem. Int. Ed.</i> <b>2023</b> , 62 (27), e202305246. <sup>16</sup> |
| RuNi-MOF                            | 50 mg L <sup>-1</sup> NO <sub>3</sub> <sup>-</sup><br>+ 0.1 M<br>Na <sub>2</sub> SO <sub>4</sub>  | 73 | 14.6 | 0.10  | -1.2  | <i>J. Mater. Chem. A.</i> <b>2022</b> , 10 (8), 3963-3969. <sup>17</sup>      |
| Cu@CuHHTP                           | 500 mg L <sup>-1</sup><br>NO <sub>3</sub> <sup>-</sup> + 0.5 M<br>Na <sub>2</sub> SO <sub>4</sub> | 68 | 35.8 | 0.108 | -1.3  | <i>J. Mater. Chem. A.</i> <b>2022</b> , 10 (8), 3963-3969. <sup>18</sup>      |
| Ni-MOF                              | 0.1 M Na <sub>2</sub> SO <sub>4</sub><br>+ 1.5 g L <sup>-1</sup><br>NaNO <sub>3</sub>             | 13 | 3.78 | 0.006 | -1.4  | <i>J. Colloid. Interf. Sci.</i> <b>2023</b> , 638, 26-38. <sup>19</sup>       |
| Zr-MOF                              | 500 mg L <sup>-1</sup><br>NO <sub>3</sub> <sup>-</sup> + 0.1 M<br>Na <sub>2</sub> SO <sub>4</sub> | 58 | 23   | 0.29  | -1.6  | <i>Nano Lett.</i> <b>2022</b> , 22 (6), 2529-2537. <sup>20</sup>              |
| CuPd aerogels                       | 0.5 M K <sub>2</sub> SO <sub>4</sub> +<br>50 mg L <sup>-1</sup> NO <sub>3</sub> <sup>-</sup><br>N | 90 | 7.4  | 0.046 | -0.87 | <i>Nano Lett.</i> <b>2022</b> , 22 (6), 2529-2537. <sup>21</sup>              |
| plasma treated<br>Cu <sub>2</sub> O | 0.5 M Na <sub>2</sub> SO <sub>4</sub><br>+ 50 mg L <sup>-1</sup><br>NaNO <sub>3</sub> -N          | 90 | 22.4 | 0.024 | -1.0  | <i>Nano Lett.</i> <b>2022</b> , 22 (6), 2529-2537. <sup>22</sup>              |

**Table S6.** Elemental analysis of  $\text{Cu}_3(\text{PyCA})_3$ .

| Element   | C     | N     | H    | Cu    |
|-----------|-------|-------|------|-------|
| Found (%) | 32.69 | 17.49 | 1.72 | 38.17 |
| Calc. (%) | 30.18 | 17.61 | 1.89 | 40.25 |

**Table S7.** Elemental analysis of  $\text{Cu}_3(\text{Me-PyCA})_3$ .

| Element   | C     | N     | H    | Cu    |
|-----------|-------|-------|------|-------|
| Found (%) | 39.87 | 15.32 | 3.92 | 31.89 |
| Calc. (%) | 39.05 | 15.00 | 3.86 | 34.14 |

**Figure S23.** (a) The PXRD patterns of  $\text{Cu}_3(\text{PyCA})_3$  and  $\text{Cu}_3(\text{Me-PyCA})_3$ , respectively. (b) FT-IR spectra for  $\text{Cu}_3(\text{PyCA})_3$  and  $\text{Cu}_3(\text{Me-PyCA})_3$ .

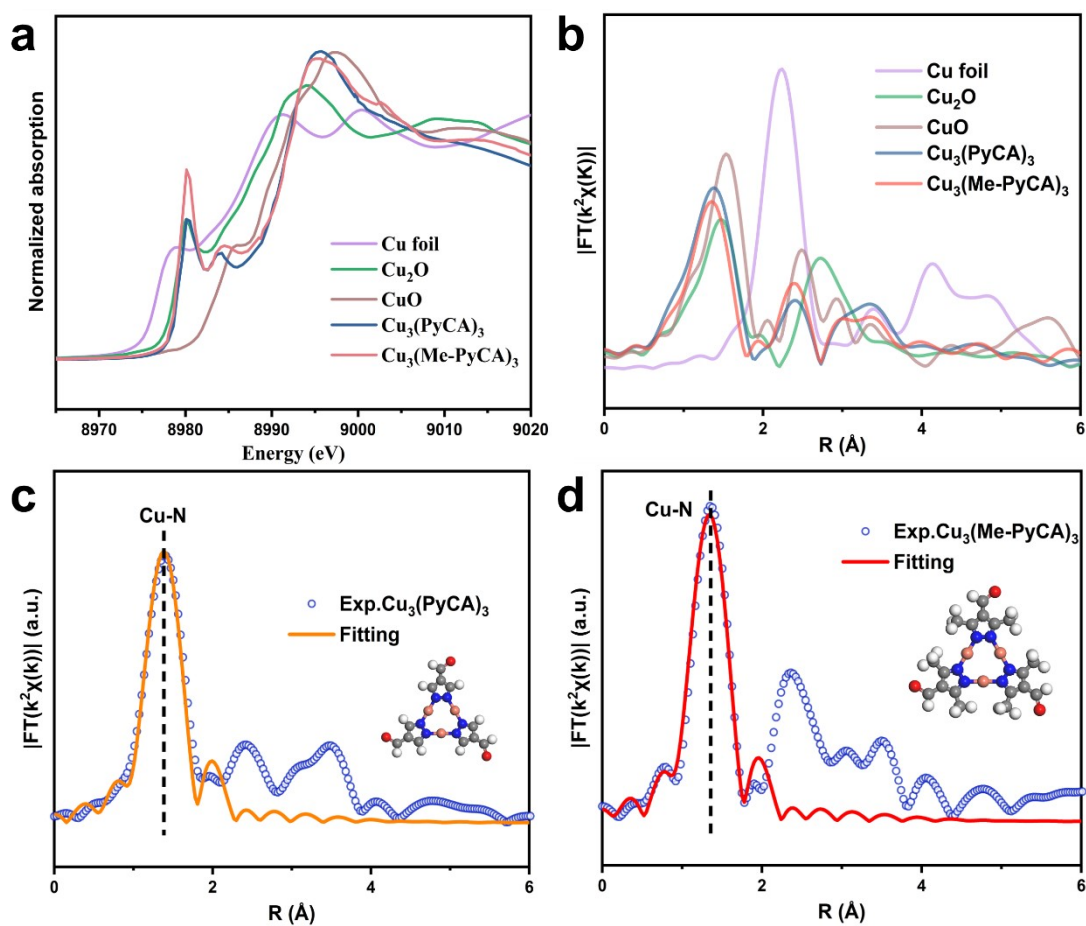


**Figure S24.** (a) Cu K-edge of XANES spectra of Cu<sub>3</sub>(PyCA)<sub>3</sub>, Cu<sub>3</sub>(Me-PyCA)<sub>3</sub>, Cu foil, CuO and Cu<sub>2</sub>O. (b) Cu K-edge of EXAFS spectra of Cu<sub>3</sub>(PyCA)<sub>3</sub>, Cu<sub>3</sub>(Me-PyCA)<sub>3</sub>, Cu foil, CuO and Cu<sub>2</sub>O. (c) The EXAFS fitting curves of Cu<sub>3</sub>(PyCA)<sub>3</sub>. (d) The EXAFS fitting curves of Cu<sub>3</sub>(Me-PyCA)<sub>3</sub>.

**Table S8.** Cu K-edge EXAFS curve fitting parameters of  $\text{Cu}_3(\text{PyCA})_3$  and  $\text{Cu}_3(\text{Me-PyCA})_3$ . CN, coordination number; R, distance between absorber and backscatter atoms;  $\sigma^2$ , Debye-Waller factor (a measure of thermal and static disorder in absorber-scatterer distances); R factor is used to value the goodness of the fitting.

| <b>Sample</b>                   | <b>Path</b> | <b>CN</b> | <b>R (Å)</b> | <b><math>\sigma^2</math> (<math>10^{-3}</math> Å<sup>2</sup>)</b> | <b>R factor</b> |
|---------------------------------|-------------|-----------|--------------|---|-----------------|
| $\text{Cu}_3(\text{PyCA})_3$    | Cu-N        | 2         | 1.85         | 5.0±3.1   | 0.02            |
| $\text{Cu}_3(\text{Me-PyCA})_3$ | Cu-N        | 2         | 1.82         | 5.9±3.2   | 0.01            |

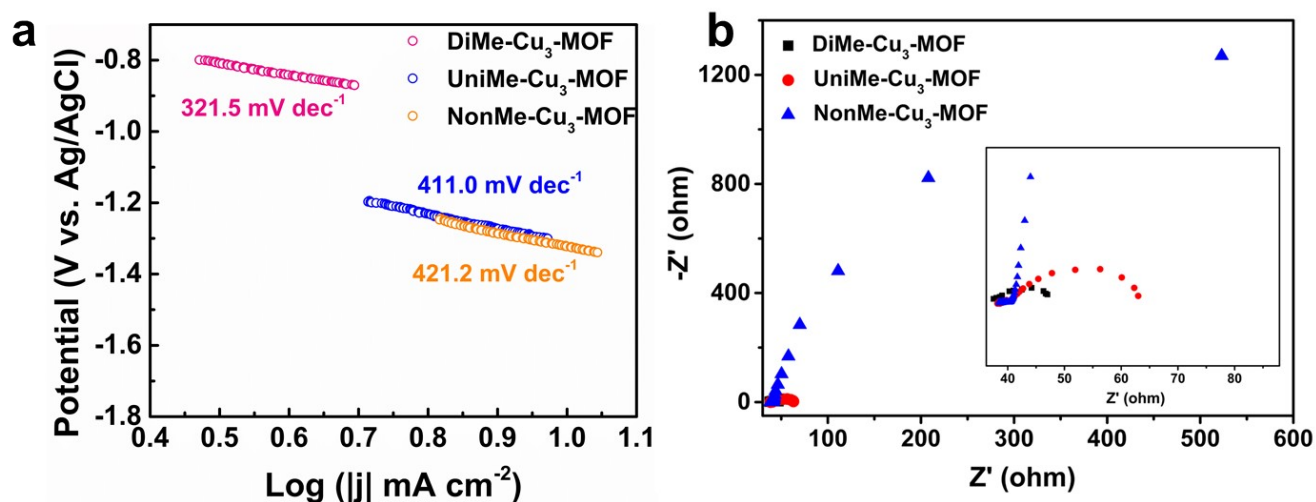


**Figure S25.** (a) Tafel slopes of NO<sub>3</sub>RR over DiMe-Cu<sub>3</sub>-MOF, NonMe-Cu<sub>3</sub>-MOF and UniMe-Cu<sub>3</sub>-MOF. (b) The electrochemical impedance spectroscopy Nyquist plots of DiMe-Cu<sub>3</sub>-MOF, NonMe-Cu<sub>3</sub>-MOF and UniMe-Cu<sub>3</sub>-MOF.

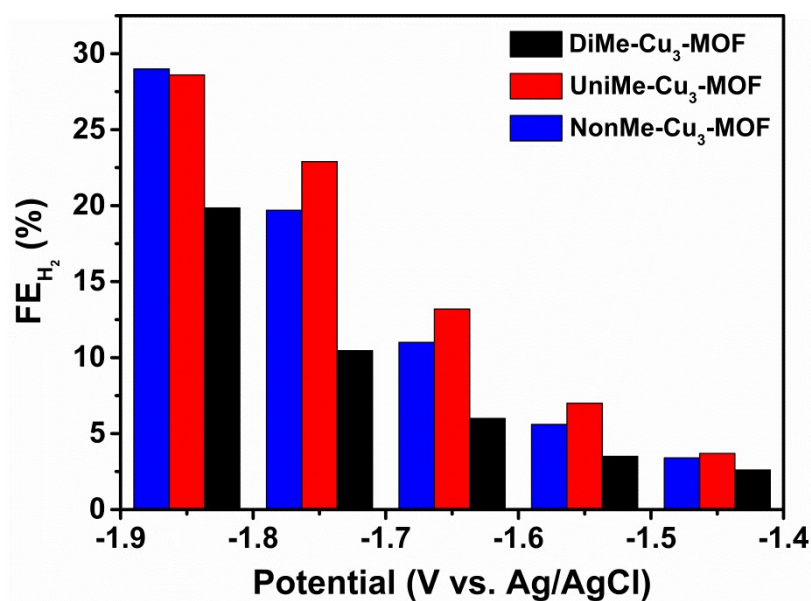


**Figure S26.** The HER of DiMe-Cu<sub>3</sub>-MOF, NonMe-Cu<sub>3</sub>-MOF and UniMe-Cu<sub>3</sub>-MOF under 0.5 M K<sub>2</sub>SO<sub>4</sub> and 50 mM KNO<sub>3</sub> electrolytes.

## References

1. G. Kresse and J. Furthmüller, Efficiency of ab-initio total energy calculations for metals and semiconductors using a plane-wave basis set, *Comp. Mater. Sci.*, 1996, **6**, 15-50.
2. G. Kresse and J. Furthmüller, Efficient iterative schemes for ab initio total-energy calculations using a plane-wave basis set, *Phys. Rev. B*, 1996, **54**, 11169-11186.
3. G. Kresse and J. Hafner, Ab initio molecular dynamics for liquid metals, *Phys. Rev. B*, 1993, **47**, 558-561.
4. G. Kresse and J. Hafner, Ab initio molecular-dynamics simulation of the liquid-metal--amorphous-semiconductor transition in germanium, *Phys. Rev. B*, 1994, **49**, 14251-14269.
5. G. Kresse and D. Joubert, From ultrasoft pseudopotentials to the projector augmented-wave method, *Phys. Rev. B*, 1999, **59**, 1758-1775.
6. P. E. Blöchl, Projector augmented-wave method, *Phys. Rev. B*, 1994, **50**, 17953-17979.
7. J. P. Perdew, K. Burke and M. Ernzerhof, Generalized Gradient Approximation Made Simple, *Phys. Rev. Lett.*, 1996, **77**, 3865-3868.
8. S. Grimme, Density functional theory with London dispersion corrections, *WIRES. Comput. Mol. Sci.*, 2011, **1**, 211-228.
9. J. K. Nørskov, J. Rossmeisl, A. Logadottir, L. Lindqvist, J. R. Kitchin, T. Bligaard and H. Jónsson, Origin of the Overpotential for Oxygen Reduction at a Fuel-Cell Cathode, *J. Phys. Chem. B*, 2004, **108**, 17886-17892.
10. V. Wang, N. Xu, J. C. Liu, G. Tang and W. Geng, VASPKIT: A user-friendly interface facilitating high-throughput computing and analysis using VASP code, *Comput. Phys. Commun.*, 2019, **267**, 108033.
11. S. I. G. P. Mohamed, S. Namvar, T. Zhang, H. Shahbazi, Z. Jiang, A. M. Rappe, A. Salehi - Khojin and S. Nejati, Vapor - Phase Synthesis of Electrocatalytic Covalent Organic Frameworks, *Adv. Mater.*, 2023, **36**, 2309302.
12. H. Huang and K. Wang, Conductive metal-covalent organic frameworks as novel catalytic platforms for reduction of nitrate to ammonia, *Green. Chem.*, 2023, **25**, 9167-9174.
13. Z. Li, L. Wang, Y. Cai, J.-R. Zhang and W. Zhu, Electrochemically reconstructed copper-polypyrrole nanofiber network for remediating nitrate-containing water at neutral pH, *J. Hazard. Mater.*, 2022, **440**, 129828.
14. Y. Zhao, Y. Liu, Z. Zhang, Z. Mo, C. Wang and S. Gao, Flower-like open-structured polycrystalline copper with synergistic multi-crystal plane for efficient electrocatalytic reduction of nitrate to ammonia, *Nano Energy*, 2022, **97**, 107124.
15. Y. Wang, W. Zhou, R. Jia, Y. Yu and B. Zhang, Unveiling the Activity Origin of a Copper-based Electrocatalyst for Selective Nitrate Reduction to Ammonia, *Angew. Chem. Int. Ed.*, 2020, **59**, 5350-5354.
16. Y. Lv, S.-W. Ke, Y. Gu, B. Tian, L. Tang, P. Ran, Y. Zhao, J. Ma, J.-L. Zuo and M. Ding, Highly Efficient Electrochemical Nitrate Reduction to Ammonia in Strong Acid Conditions with Fe<sub>2</sub>M-Trinuclear-Cluster Metal–Organic Frameworks, *Angew. Chem. Int. Ed.*, 2023, **62**, e202305246.
17. J. Qin, K. Wu, L. Chen, X. Wang, Q. Zhao, B. Liu and Z. Ye, Achieving high selectivity for nitrate electrochemical reduction to ammonia over MOF-supported Ru<sub>x</sub>O<sub>y</sub> clusters, *J. Mater. Chem. A*, 2022, **10**, 3963-3969.
18. X. Zhu, H. Huang, H. Zhang, Y. Zhang, P. Shi, K. Qu, S.-B. Cheng, A.-L. Wang and Q. Lu, Filling Mesopores of Conductive Metal–Organic Frameworks with Cu Clusters for Selective Nitrate Reduction to Ammonia, *ACS Appl. Mater. Interfaces*, 2022, **14**, 32176-32182.
19. F. Pan, J. Zhou, T. Wang, Y. Zhu, H. Ma, J. Niu and C. Wang, Revealing the activity origin of ultrathin nickel metal–organic framework nanosheet catalysts for selective electrochemical nitrate reduction to ammonia: Experimental and density functional theory investigations, *J. Colloid. Interf. Sci.*, 2023, **638**, 26-38.
20. M. Jiang, J. Su, X. Song, P. Zhang, M. Zhu, L. Qin, Z. Tie, J.-L. Zuo and Z. Jin, Interfacial Reduction Nucleation of Noble Metal Nanodots on Redox-Active Metal–Organic Frameworks for High-Efficiency Electrocatalytic Conversion of Nitrate to Ammonia, *Nano Lett.*, 2022, **22**, 2529-2537.
21. Y. Xu, K. Ren, T. Ren, M. Wang, M. Liu, Z. Wang, X. Li, L. Wang and H. Wang, Cooperativity of Cu and Pd active sites in CuPd aerogels enhances nitrate electroreduction to ammonia, *Chem. Commun*, 2021, **57**, 7525-7528.

22. Z. Gong, W. Zhong, Z. He, Q. Liu, H. Chen, D. Zhou, N. Zhang, X. Kang and Y. Chen, Regulating surface oxygen species on copper (I) oxides via plasma treatment for effective reduction of nitrate to ammonia, *Appl. Catal. B-Environ*, 2022, **305**, 121021.